CHEMISTRY OF MATERIALS

pubs.acs.org/cm

Article

Element-Selective Analysis of Carrier Behavior in Plasmonic Metal−Zinc Oxide (M = Al or Ga) Nanocrystals

Robert B. Smith,[§] Carl R. Conti, III,[§] Sarah D. Bennett, Adam R. Altenhof, Geoffrey F. Strouse,* and Robert W. Schurko*

Cite This: *Chem. Mater.* 2025, 37, 6962−6973

Read Online

ACCESS | Metrics & More | Article Recommendations | Supporting Information

ABSTRACT: The ability to correlate changes in free carrier densities with changes in atomic structure in plasmonic semiconducting nanocrystals (NCs) can improve our understanding of these materials and lend insight into their rational design. Zinc oxide (ZnO) is of particular interest in this class of materials because of its uniquely wide band gap, which can be manipulated through the addition of dopants (e.g., Al^{3+} and Ga^{3+}). Herein, we demonstrate the utility of solid-state NMR (SSNMR) in tandem with other spectroscopic techniques to probe changes in atomic structure and elucidate the relationship between these changes and free carrier densities in a series of ZnO NCs doped with varying concentrations of Al^{3+} and Ga^{3+} (i.e., AZO and GZO, respectively). ^{67}Zn SSNMR is employed to draw comparisons between the bulk ZnO phase and the ZnO NC phases. ^{67}Zn SSNMR is also employed to study how differences in dopant size and concentration affect dopant deactivation and, hence, free carrier densities and the resulting frequency of the plasmon. ^{27}Al and ^{71}Ga SSNMR are employed to probe the effects of dopant incorporation on the zinc oxide lattice and gain insight into the preferred coordination environments of each dopant. In the AZO NCs, four-, five-, and six-coordinate Al^{3+} environments are observed, whereas in the GZO NCs, only four- and six-coordinate Ga^{3+} environments are identified. In both, higher doping levels result in increased dopant populations in six-coordinate environments. These samples also exhibit the largest distributions of ^{67}Zn Knight shifts, which is consistent with the highest carrier densities determined from fitting mid-IR localized surface plasmon resonance (LSPR) extinction spectra, inferring that the nature and populations of the dopants play important roles in their determination. This raises the tantalizing possibility of using such information to rationally design new types of NCs with tunable carrier densities and LSPR frequencies.

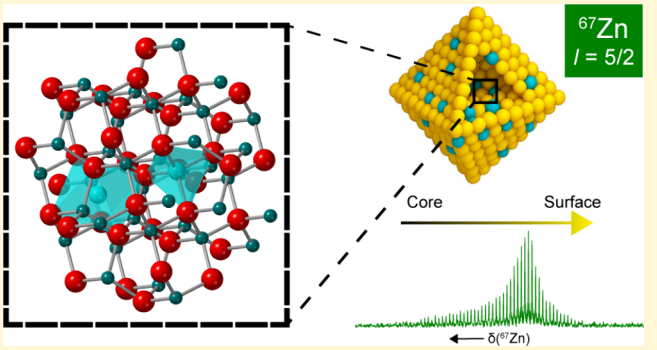

1. INTRODUCTION

The sizes, shapes, surface modifications, and compositional dependences of intentionally doped nanocrystals (NCs) and nanoparticles (NPs) are widely studied for their magnetic, photonic, electronic, catalytic, and pharmaceutical applications.[1−7] Zinc oxide (ZnO) NCs are a class of materials that have seen widespread use in the field of optoelectronics, since ZnO is an intrinsic *n*-type semiconductor (i.e., *n*-type behavior exists without the addition of dopants) with a uniquely wide band gap (~3.4 eV) that allows for the safe conduction of high amperage currents for extended periods of time. Furthermore, ZnO is composed of earth-abundant elements with a band structure that can be tuned to be *n*-type by photodoping or doping with group IIIA and IVA elements.[8] The incorporation of group III/IVA elements into the ZnO lattice leads to formation of *n*-type carriers in the conduction band, reflecting the location of the Fermi level with increasing donor content.[9] Aliovalent doping of ZnO with group IIIA metals, such as Al, Ga, and In, provides an advantage over photodoping in that the materials are intrinsically plasmonic and do not require a hole scavenger to generate free carriers (i.e., conducting electrons in *n*-type semiconductors). In ZnO NCs, *n*-doping with group IIIA elements can generate carrier densities between 10^{19} and 10^{21} carriers cm^{-3}, which has been shown to induce metallic character in these wide band gap semiconductors, with a plasmon resonance in the mid-infrared that follows classical Drude behavior.[10,11] In addition to this, changes in the bandgap absorption energy arise, which is consistent with the Mossec−Burstein effect.[12]

In a recent study, it was shown that the range of frequency and intensity tuning of the plasmon feature in ZnO NCs is

Received: February 28, 2025
Revised: August 21, 2025
Accepted: August 22, 2025
Published: September 5, 2025

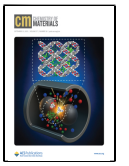

https://doi.org/10.1021/acs.chemmater.5c00496
Chem. Mater. 2025, 37, 6962−6973

limited by the formation of compensation centers at concentrations above 5%.[13] The compensation centers may arise from the presence of deactivated carriers through a surface depletion layer, defect-mediated pinning of free carriers, or inclusion of insulating microphases. Previous studies of metal-doped zinc oxide (MZO) NCs via far-field optical measurements support the role of surface depletion for carrier deactivation;[14] however, no direct evidence of the defect sites can be provided from absorption data. In a recent study, comparison of 10 nm ZnO NCs doped with Al^{3+}, Ga^{3+}, and In^{3+} (i.e., AZO, GZO, and IZO), revealed that compensation center formation is concentration-dependent and correlates with the size of the group III element.[14] Better dopant/host size matching leads to increases in both the efficiency of aliovalent substitution and free carrier density, which, in turn, lead to an increase in the localized surface plasmon resonance (LSPR) frequency of the NCs. The LSPR energies of MZO nanocrystals increase with higher group III dopant concentrations and also progressively rise from aluminum to gallium to indium at fixed doping levels, suggesting changes in carrier effective mass or orbital overlap associated with dopant size.[14]

Although *n*-type MZO NCs are widely studied, the sites of dopant incorporation that lead to carrier formation in the conduction band have not been thoroughly explored (i.e., whether the onset of compensation centers is a surface phenomenon or the result of dopant site occupation in the lattice). In order to rationally design MZO NCs with specific physicochemical attributes, a thorough understanding of the relationships between structure, properties, and function (SPF) is required. Numerous characterization techniques can be used to evaluate such relationships in inorganic NPs and NCs, including transmission electron microscopy (TEM), powder X-ray diffraction (pXRD), differential scanning calorimetry (DSC), X-ray photoelectron spectroscopy (XPS), X-ray absorption spectroscopy (XAS), electron paramagnetic resonance (EPR), and cyclic voltammetry (CV). Correlation of results from these methods provide useful information on NC size, structure, and physicochemical properties (e.g., oxidation state, vacancies, dopant concentration, band gap structure, and NC size distribution); however, in most cases, they do not provide atomic-level resolution of the chemical environments in NCs, which is crucial for studying SPF relationships.[15]

In this respect, solid-state NMR (SSNMR) spectroscopy plays an important role, as it provides an element-specific structural probe of local atomic environments, both within the core and on the surface of the NC, as well as information on surface−ligand bonding, molecular-level dynamics, and short- and long-range structural order. Furthermore, SSNMR experiments are capable of measuring both isotropic and anisotropic NMR interactions, with the former offering opportunities for site assignments and general characterization of coordination environments and the latter often yielding rich detail on symmetry and/or electronic structure.

There are several anisotropic NMR interactions that influence the SSNMR spectra of nuclides of main group and transition metal elements. The SSNMR spectra of spin $I = 1/2$ nuclides from these groups are often influenced by large chemical shift anisotropies (CSAs), which are strongly dependent upon short-range (i.e., covalent, or dative) bonding interactions. The SSNMR spectra of quadrupolar nuclei (i.e., $I > 1/2$) are additionally influenced by quadrupolar interactions (QI), which are highly sensitive to changes in local symmetry as well as weaker bonding interactions (i.e., ionic, hydrogen bonding, and van der Waals interactions). Finally, in materials with conduction electrons, it is often possible to observe the manifestation of Knight shifts and/or Knight shift anisotropy (KSA) in SSNMR spectra, which often give rise to SSNMR powder patterns with unusually high or low shifts and extreme broadening beyond conventional chemical shifts or CSAs in diamagnetic materials, respectively (see Supplement S1).[16−19] It is worth noting that solution NMR cannot usually elicit similar information, since the slow molecular tumbling of NPs in solution leads to short T_2 relaxation times and large peak widths, while also serving to completely or partially average anisotropic interactions.[20] As such, the interrogation of the dopant site occupation in MZO NCs by SSNMR could aid in developing an increased understanding of the chemical origins of carrier formation and compensation. Recent reports have shown the power of SSNMR methods for investigating dopant site occupation and carrier-induced Knight shift behavior in *n*-ITO, *p*-$Cu_{1-x}Se$, and Cd_2SnO_4 plasmonic NCs, via elucidation of the site occupation by different elements and observation of Knight shifts that provide evidence of metallic character.[21−26]

Herein, we demonstrate the utility of ^{67}Zn ($I = 5/2$), ^{27}Al ($I = 5/2$), and ^{71}Ga ($I = 3/2$) SSNMR to correlate LSPR properties with dopant concentrations in 13 nm AZO and 10 nm GZO spherical NCs passivated with oleic acid. ^{67}Zn SSNMR experiments are used to compare the atomic-level structures of bulk ZnO and ZnO NCs, observe Knight shifts that are dependent upon dopant concentrations, and discern the possible onset of Al(III)-V_O-Al(III) and Ga(III)-V_O-Ga(III) spinel like inclusions (i.e., ZnM_2O_4, M = Al and Ga) at higher dopant concentrations that may lead to partial carrier deactivation. These Knight shifts can be correlated with the observed plasmon and bandgap energies measured with mid-IR spectroscopic methods and discussed in the context of the generation of free carriers and the density of states. Finally, ^{27}Al and ^{71}Ga SSNMR experiments are used to probe the coordination environments of the Al^{3+} and Ga^{3+} dopants in the AZO and GZO NCs, respectively, to determine relationships among these environments, their concentrations, and the free carrier densities.

2. MATERIALS AND METHODS

Aluminum(III) acetylacetonate ($Al(acac)_3$, 99.99%), oleic acid (90%, technical grade), and tetrachloroethylene (spectrophotometric grade, 99+%) were purchased from Alfa Aesar (Ward Hill, MA). Gallium(III) nitrate hydrate ($Ga(NO_3)_3{\cdot}H_2O$, ≥99.9998%) was purchased from Acros Organics (Fair Lawn, NJ). Oleyl alcohol (80−85%, technical grade), gallium(III) acetylacetonate ($Ga(acac)_3$, ≥99.99%), and aluminum(III) nitrate nonahydrate ($Al(NO_3)_3{\cdot}9H_2O$, ≥99.999%) were purchased from Beantown Chemical (Hudson, NH). Ethanol (95%) and nitric acid (67−70%, for trace metal analysis) were purchased from VWR (Suwanee, GA). Toluene (≥99.5%), oleylamine (70%), zinc(II) acetate dihydrate ($Zn(OAc)_2{\cdot}2H_2O$, ≥98%), and zinc(II) nitrate hexahydrate ($Zn(NO_3)_2{\cdot}6H_2O$, ≥99%) were purchased from Sigma-Aldrich (St. Louis, MO).

2.1. Synthesis of MZO Nanocrystals. 13 nm AZO and 10 nm GZO spherical NCs passivated with oleic acid were synthesized as previously reported, using a modified method of Della Gaspera and co-workers.[14,27] Briefly, metal oleate stock solutions with various mole ratios of $Al(acac)_3$ or $Ga(acac)_3$ to $Zn(OAc)_2$ were prepared in a 1:2 (V:V) mixture of oleic acid to oleylamine at 110 °C. The nucleation and growth of the MZO NCs are accomplished by dropwise (0.3 mL/min) addition of 15 mL of the metal oleate stock solution to 62.5 mL of oleyl alcohol at 240 °C under anaerobic conditions (N_2). After the injection is complete, the solution is kept at 240 °C for an additional

https://doi.org/10.1021/acs.chemmater.5c00496
Chem. Mater. 2025, 37, 6962−6973

Table 1. Extended Drude Model Fits for AZO and GZO NCs

	% dopant (mol %)	ω_p[a] (cm^{-1})	carrier density, n[b] (carriers/cm^3)	ω_{LSPR}[b] (cm^{-1})	carrier activation[c] (%)
AZO	0.9	5037 ± 20	6.51×10^{19}	1883	3.4
	2.1	5142 ± 20	6.78×10^{19}	2103	1.5
	4.3	5221 ± 20	6.99×10^{19}	1977	0.76
	9.6	5257 ± 20	7.09×10^{19}	2056	0.35
GZO	2.1	5209 ± 20	6.96×10^{19}	2226	1.6
	6.5	5364 ± 20	7.38×10^{19}	2324	0.54
	10.3	5458 ± 20	7.64×10^{19}	2399	0.35
	17.9	5588 ± 20	8.01×10^{19}	2446	0.21

[a]ω_p is extracted by fitting the background corrected optical data to the extended Drude model (SXDA) by fitting to a high and low frequency dielectric constant. Error analysis is performed by evaluating the shift in ω_p by varying the initial dielectric constant values in the SXDA fits. The fitting parameters are available in Table S5. [b]From ω_p, the values of ω_{LSPR} and n are extracted using the Drude−Lorentz approximation assuming a constant value of m^* (n-ZnO, $0.23m_e$) and the values obtained for the low and high frequency dielectric constants from the SXDA fit. All fits are performed on background corrected extinction data to account for sharp features associated with the quartz optical cell, absorption from the passivating ligand, and detector cutoff at low frequency. [c]The efficiency of carrier activation is determined by comparing the calculated number of carriers per NC to the theoretical maximum based on full activation.[21]

20 min, followed by cooling to room temperature and isolation/cleanup of the NCs using toluene/ethanol (3×) and centrifugation.

2.2. Elemental Analysis. Inductively coupled plasma mass spectrometry (ICP-MS) was performed using a Thermo Scientific iCAP RQ ICP-MS to confirm the ratio of (Al/Ga):Zn in the NCs. Samples were digested in concentrated nitric acid and then diluted to 2% HNO_3. Calibration curves were prepared from serial dilutions of an Al/Ga/Zn standard dissolved in 2% HNO_3 with R^2 values >0.995 for all ions. Each sample was measured in triplicate after an initial survey run, with a minimum 30 s wash time between samples.

2.3. Powder X-ray Diffraction. pXRD patterns were collected with a Rigaku MiniFlex powder X-ray diffractometer using a Cu-Kα. Samples were dried out and crushed into a fine powder and then loaded onto a zero-background micropowder plate. Scans were collected from 20° to 70° 2θ at a rate of 5°/min and a 0.1° step size. Whole powder pattern fits were performed for all NCs using the Halder−Wagner method to determine NC size using the Rigaku SmartLab Studio software.

2.4. Fourier-Transform Infrared Spectroscopy. Purified MZO NCs were suspended in tetrachloroethylene and diluted to the appropriate concentrations. Samples were then loaded into a Pike Technologies Liquid FTIR cell with BaF_2 windows and a path length of 0.5 mm. FTIR measurements were performed in transmission mode by using a Jasco 6800 FTIR spectrometer. The LSPR feature is fit to a simplified Drude approximation by assuming a Lorentzian function. To fit the LSPR feature, the sharp ligand and solvent modes observable in the sample are fit through comparison to published ligand FTIR spectra.[28]

2.5. Solid-State NMR Spectroscopy. ^{67}Zn NMR experiments were performed using a Bruker AVANCE III console with an Oxford 19.6 T ($\nu_0(^1H)$ = 830 MHz) magnet operating at $\nu_0(^{67}Zn)$ = 51.931 MHz. ^{27}Al NMR experiments were performed by using a Bruker NEO console with an Oxford 18.8 T ($\nu_0(^1H)$ = 800 MHz) magnet operating at $\nu_0(^{27}Al)$ = 208.455 MHz. ^{71}Ga NMR experiments were performed using a Bruker AVANCE NEO console with an Oxford 14.1 T ($\nu_0(^1H)$ = 600 MHz) magnet, Bruker NEO console with an Oxford 18.8 T ($\nu_0(^1H)$ = 800 MHz) magnet, and Bruker NEO console with the in-house built 35.2 T Series Connected Hybrid (SCH) ($\nu_0(^1H)$ = 1.5 GHz) magnet operating at $\nu_0(^{71}Ga)$ = 182.980 MHz, $\nu_0(^{71}Ga)$ = 243.974 MHz, and $\nu_0(^{71}Ga)$ = 467.411 MHz, respectively.[29]

A 3.2 mm HX magic angle spinning (MAS) probe was used for ^{67}Zn experiments, an HX low-E static probe was used for ^{71}Ga experiments performed at 11.7 T, a 3.2 mm HXY MAS probe was used for ^{71}Ga and ^{27}Al experiments performed at 18.8 T, and a 3.2 mm HX MAS probe was used for experiments performed at 35.2 T. All of these NMR probes were designed and built in-house at MagLab.

All ^{67}Zn experiments were carried out using the QCPMG pulse sequence,[30,31] which is of the form $\pi/2 - \tau - [\pi - \tau - \text{acq}]_n$, where the $\pi/2$ and π pulses are central-transition (+1/2 ↔ −1/2) selective,[32] τ are interpulse delays, acq is the acquisition window, and n is the number of CPMG loops (as permitted by the effective T_2). Only seven spin echoes were acquired for all samples due to short transverse relaxation times. Spectra were processed using a Fourier transform followed by a magnitude calculation in order to yield "spikelet" spectra, which improves signal-to-noise (S/N).[33]

All ^{27}Al SSNMR experiments were carried out using the Hahn-echo pulse sequence[34] under MAS conditions using rotor-synchronized, central-transition selective pulses. Spectra were processed using a Fourier transform followed by application of zeroth and first order phasing to yield absorptive spectra.

^{71}Ga SSNMR experiments were carried out using the QCPMG pulse sequence under both static and MAS conditions as appropriate (e.g., when resolution improvement was necessary for site assignment). Spectra were processed using a Fourier transform followed by a magnitude correction with the same rationale as for the aforementioned ^{67}Zn SSNMR experiments. ^{71}Ga 2D quadrupolar magic-angle turning (QMAT) experiments were carried out at 35.2 T in order to aid in the resolution of distinct powder patterns.[35]

Pulse width calibrations and chemical shift reference frequencies for all nuclei were determined using their respective solution-state standards, with ^{67}Zn, ^{27}Al, and ^{71}Ga chemical shifts referenced to 1.0 M $Zn(NO_3)_2$, 1.0 M $Al(NO_3)_3$, and 1.0 M $Ga(NO_3)_3$, respectively, with all primary standards set to δ_{iso} = 0.0 ppm. High-power ^{1}H decoupling was used in every experiment. Details on this and other experimental conditions and acquisition parameters for each experiment are summarized in Tables S1−S3.

2.6. Spectral Processing and Simulations. Data were acquired and processed using TopSpin 4.1.1 software. Numerical simulations and spectral fits were performed using the ssNake software package.[36]

3. RESULTS AND DISCUSSION

3.1. Synthesis and Basic Characterization. All the MZO NCs (M = Al, Ga) were isolated as spherical, oleic acid passivated NCs crystallizing in the ZnO hexagonal wurtzite phase (PDF #036-1451) (Figures S1−S3).[14] Elemental composition was ascertained by ICP-MS (Table S4). The carrier concentration- and dopant-dependent LSPR extinction spectra measured using FTIR are provided in the ESI (Figures S4 and S5). The carrier density is evaluated by fitting the background subtracted short-wave mid-IR (SWIR) extinction spectra to the Extended Drude Model (SXDA)[28] using a reduced electron mass of m^* = $0.23m_e$. The experimental carrier densities derived from fits utilizing SXDA for the isolated MZO samples, in addition to ω_p and ω_{LSPR}, are

https://doi.org/10.1021/acs.chemmater.5c00496
Chem. Mater. 2025, 37, 6962−6973

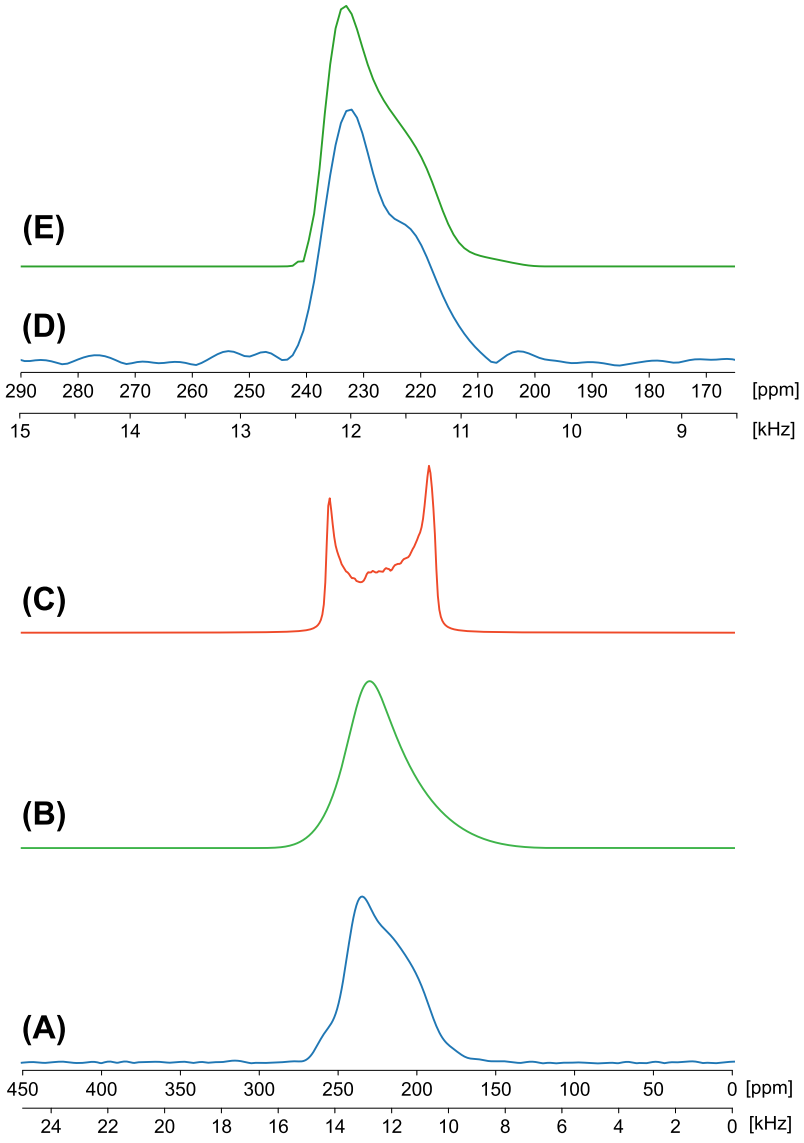

Figure 1. (A) Experimental ^{67}Zn SSNMR spectrum of undoped ZnO NCs acquired at 19.6 T under static conditions. Corresponding simulations of ^{67}Zn SSNMR spectra of (B) ZnO NCs and (C) bulk ZnO based on a Czjzek distribution model. (D) Experimental ^{67}Zn SSNMR spectrum of undoped ZnO NCs acquired at 19.6 T under MAS (ν_{rot} = 12 kHz) conditions. (E) Corresponding simulation based on a Czjzek distribution model.

summarized in Table 1. The degree of carrier activation is evaluated using the ω_p values extracted from SXDA to estimate the number of carriers per NC, and comparison of these values to the theoretical number of carriers is based upon composition analysis (Table 1). In all samples, carrier activation is observed to decrease with increasing Al^{3+} and Ga^{3+} content. The observed decrease in carrier activation is consistent with the possible presence of a significant surface depletion layer, the presence of phase segregation, or the formation of inactive M-V_O-M (M = Al or Ga) pairs within the ZnO NC. Additional fitting parameters derived from SXDA are given in Table S5. SXDA fits are generated using the MATLAB code of Milliron et al.[28]

3.2. Multinuclear Solid-State NMR Characterization. *3.2.1. Challenges with ^{67}Zn SSNMR Spectroscopy.* Acquisition of ^{67}Zn SSNMR spectra is made difficult by the NMR properties of ^{67}Zn, including its low natural abundance (4.1%), moderate quadrupole moment (Q = 15.0 fm^2), and relatively low gyromagnetic ratio (1.67669×10^7 rad T^{-1} s^{-1}). In this work, the QCPMG experiment is used, which entails acquisition of a train of spin echoes for as long as the effective T_2 allows. Long values of T_2^{eff} (e.g., tens of ms or more) permit the acquisition of many echoes, which serves to increase S/N in the ^{67}Zn QCPMG spectrum.

In the presence of conduction electrons, $T_2^{eff}(^{67}Zn)$ can be shortened such that relatively few echoes can be acquired, which necessitates long experiment times. Furthermore, it is likely that different Zn sites throughout the NC have distinct Knight shifts and, hence, different values of $T_2^{eff}(^{67}Zn)$, which makes quantification of the populations of specific Zn sites speculative at best. Variable-temperature NMR experiments and T_1 relaxation measurements can be used to achieve some degree of quantification;[22,37] however, when distributions of Knight shifts are present, anisotropic distributions of T_1 relaxation times are possible, which further complicates analysis. In this work, due to the unreceptive nature of ^{67}Zn

https://doi.org/10.1021/acs.chemmater.5c00496
Chem. Mater. 2025, 37, 6962−6973

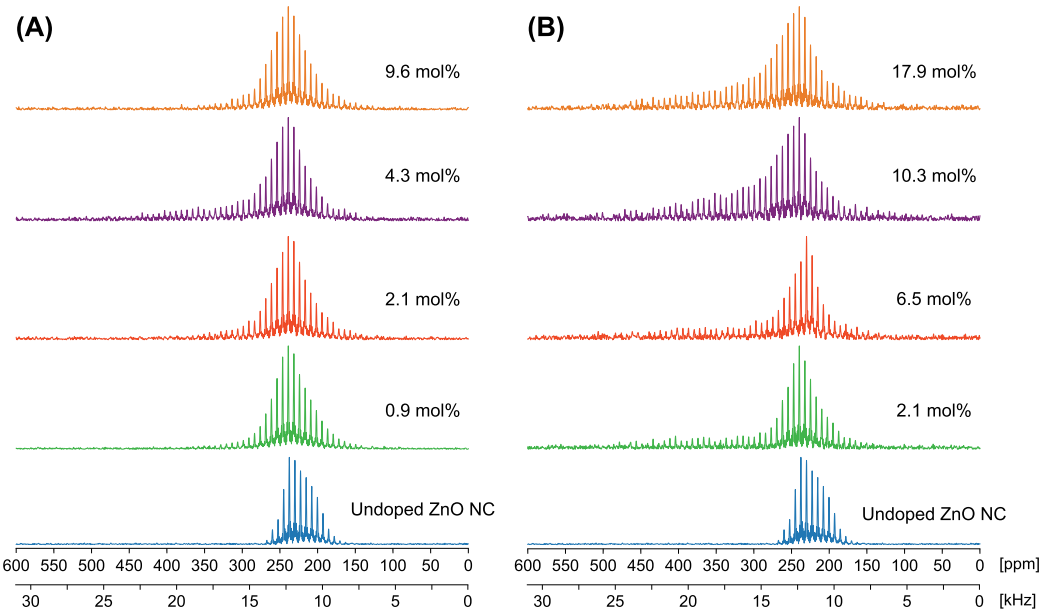

Figure 2. ^{67}Zn QCPMG NMR spectra of (A) AZO and (B) GZO NCs at varying doping levels acquired at 19.6 T under static conditions. QCPMG spectra were processed in "spikelet mode" to enhance the SNRs in the high-frequency (leftmost) portions of the spectra.

and long experiment times (*ca.* 11 h), T_1 measurements are infeasible. Nonetheless, ^{67}Zn QCPMG experiments permit mapping of the distributions of Knight shifts for a range of different samples (*vide infra*), which can lend insight into the carrier densities.

3.2.2. ^{67}Zn SSNMR: Bulk ZnO vs. Undoped ZnO NCs. The ^{67}Zn SSNMR spectrum of a stationary (static) sample of ZnO NCs with an average diameter of 10 nm (produced by coaddition of CPMG echoes) is compared to its simulation derived from a Czjzek distribution model (*vide infra*)[38−40] and a simulated spectrum of bulk ZnO (Figure 1). A similar comparison is drawn using a ^{67}Zn SSNMR spectrum of ZnO NCs acquired under MAS conditions. The central transition (CT, $+1/2 \leftrightarrow -1/2$) powder pattern of bulk, crystalline ZnO (Figure 1C) is simulated with values of C_Q = 2.5(2) MHz, η_Q = 0.05(5), δ_{iso} = 235(1) ppm, and Gaussian broadening of 100 Hz, similar to previously reported spectra that feature sharp discontinuities indicative of a microcrystalline sample.[38,39]

The ^{67}Zn SSNMR spectrum of a sample of ZnO NCs (Figure 1A) reveals a CT pattern of similar breadth to the simulation for bulk crystalline ZnO in Figure 1C, but possessing a distinct shape, which on first sight may suggest very different Zn environments between the two phases. However, this is disproved by two independent sets of data: (i) first, the centers of gravity (i.e., chemical shifts) and breadths of the CT patterns are similar for the bulk and NC phases, and (ii) pXRD patterns of bulk ZnO and ZnO NCs feature peaks occurring at identical values of 2θ (Figure S1). Since the average diameter of the undoped ZnO NC is 10 nm, there is likely a distribution of four-coordinate Zn environments, with those in the NC core similar to those of the bulk ZnO phase. Those nearer to the surface are anticipated to have environments distinct from bulk ZnO due to chemical interface reconstruction arising from coordination of Zn by oleylamine ligands on the surface. The impact of surface reconstruction on the NMR chemical shift has been reported in CdSe[41] and ZnSe[42] quantum dots and the role of the chemical interface is postulated to induce a depletion layer in metal oxide plasmonic semiconducting nanocrystals.[43]

Hence, this distribution of Zn environments can manifest in the ^{67}Zn SSNMR pattern as a distribution of isotropic shifts, δ_{iso}, quadrupolar coupling constants, C_Q, and quadrupolar asymmetry parameters, η_Q. First, the similar δ_{iso} values (*ca.* 235(1) ppm) for the CT patterns of the ZnO NCs and crystalline bulk ZnO indicate the presence of four-coordinate ZnO_4 sites (clearly, no six-coordinate Zn environments exist, as this would give rise to values of δ_{iso} near 0 ppm).[38,44] Second, the two patterns have similar breadths, indicating that there is not a broad distribution of δ_{iso} values in the ZnO NC sample. Third, this means that most of the inhomogeneous broadening is likely arising from distributions of C_Q and η_Q; hence, it should be possible to use a Czjzek model to describe the joint distribution of these parameters and obtain a spectral fit.[45] In the case of the static spectrum in Figure 1A, the Czjzek model may not be appropriate since the CT pattern may also be influenced by zinc chemical shift anisotropy (CSA), though the effects of CSA are expected to be minor in comparison to the dominant second-order quadrupolar interactions.[38,46] Hence, the Czjzek distribution model was used to fit the ^{67}Zn MAS spectrum (Figure 1D) of the ZnO NCs, from which δ_{iso} = 239(2) ppm and a Czjzek width of σ = 1.13 MHz were obtained. Assuming a most probable value of η_Q = 0.1 (from the simulation in Figure 1C), this value of σ corresponds to a root-mean-square quadrupolar product of $\langle P_Q^2\rangle^{1/2} = 5\sigma^2$ = 2.46 MHz (where $\langle P_Q^2\rangle = (C_Q^2(1 + \eta^3/3)^{1/2})$ in good agreement with that of the crystalline sample ($\langle P_Q^2\rangle^{1/2}$ = 2.5 MHz).[47] Fourth, the ^{67}Zn MAS pattern and quadrupolar parameters of the ZnO NCs are similar to those reported for the ^{67}Zn spin−echo MAS spectra acquired at 9.4 T by Spataro et al. as well as the ^{67}Zn DFS QCPMG MAS NMR spectra of Nagashima et al.[48,49] In the case of the ^{67}Zn SSNMR experiments on the doped AZO and GZO NCs herein, the static spectra are of greater value, since the CT patterns are severely broadened by Knight shifts (*vide infra*).

https://doi.org/10.1021/acs.chemmater.5c00496
Chem. Mater. 2025, 37, 6962−6973

3.2.3. ^{67}Zn SSNMR as a Probe of Free Carrier Densities in M:ZnO Samples. ^{67}Zn SSNMR spectra of AZO NCs and GZO NCs (Figure 2) were acquired for samples with different doping levels and compared to that of undoped ZnO NCs, in order to gain insight into their relationships to free carrier densities and the nature and concentration of the dopants. It is noted that (i) the spectra, which were acquired with CPMG-type sequences under static sample conditions, are processed in "spikelet mode" to maximize S/N; and (ii) the spectrum of the undoped ZnO NCs is also shown in "spikelet mode" but is derived from the same data as that in Figure 1A.

The ^{67}Zn spectra of the AZO series (Figure 2A) exhibit CT patterns that have a similar low-frequency (rightmost) distribution to that of the undoped ZnO NC sample but are much broader. Notably, the pattern skews to high frequencies (left) as the dopant concentration is increased to 4.3 mol %; the spectrum of this sample exhibits the broadest pattern width and highest intensity with respect to the low-frequency end of the pattern, with the total pattern spanning a maximum of *ca.* 290 ppm (*ca.* 15 kHz at 19.6 T). A decrease in pattern breadth and intensity is observed for the 9.6 mol % sample, comparable to that of the 2.1 mol % sample.

While part of the pattern broadening may arise from defect sites resulting from doping, the significant broadening in the high-frequency direction is attributed to Knight shifts, which arise from the presence of conduction electrons that interact with the nucleus and alter its resonant frequency, inducing a frequency shift akin to the chemical shift.[16] Since the broadening arising from Knight shift distributions is field dependent, ^{67}Zn spectra were acquired at 14.1 T were used to confirm this interpretation (Figure S6). In the case of the 4.3 mol % AZO NC sample, the signal with the highest Knight shift is at *ca.* 440 ppm, which is well above most known chemical shifts for nonmetallic Zn compounds, but well below that of Zn metal and alloys.[38] Again, this degree of broadening is highly unlikely to arise from zinc CSA, since values of Ω for four-coordinate Zn sites are generally quite small.[38,46] If $\nu_0(^{67}\mathrm{Zn})$ = 51.931 MHz corresponds to the chemical shift reference of δ_{iso} = 0.0 ppm for 1.0 M $Zn(NO_3)_2$, then the maximum Knight shifted frequency is K_{iso}^{max} = 22850 Hz (440 ppm), and the percent Knight shift is calculated as $\Delta K = K_{iso}^{max}/\nu_0(^{67}\mathrm{Zn}) \cdot 100\% = 0.044\%$.[16,50] For comparison, K_{iso} = 1770 ppm and ΔK = 0.18% for Zn metal.[51] ΔK values for other MZO samples are given in Table 2.

Table 2. Calculated ΔK Values for All X% AZO and GZO Samples and Statistical Analysis of ^{67}Zn SSNMR Spectra

	% dopant (mol %)	K_{iso}^{max} (ppm)[a]	ΔK (%)[b]	γ[c]	γ_2[d]	γ_2-3[e]
AZO NCs	0.9	360	0.036	0.40	4.29	1.29
	2.1	370	0.037	0.40	3.97	0.97
	4.3	440	0.044	1.01	3.79	0.79
	9.6	380	0.038	0.40	3.97	0.97
GZO NCs	2.1	460	0.046	1.20	3.77	0.77
	6.5	475	0.048	1.04	3.38	0.38
	10.3	485	0.048	0.83	3.05	0.05
	17.9	465	0.046	0.73	3.21	0.21

[a]The K_{iso}^{max} is the highest observed Knight shifted signal in the spectrum. [b]The percent Knight shift is calculated from $\Delta K = K_{iso}^{max}/\upsilon_0 \times 100\%$. [c]Skewness, $\gamma = \frac{\sum_i p_i(x_i-\mu)^3}{\sigma^3}$ [d]Kurtosis, $\gamma_2 = \frac{\sum_i p_i(x_i-\mu)^4}{\sigma^4}$ [e]Excess kurtosis = $\gamma_2 - 3$.

The observed Knight shifts arise because the ZnO conduction band is composed primarily of Zn 4s orbitals and the Fermi level lies in the conduction band in *n*-type plasmonic semiconductors (i.e., the presence of *s*-character at the Fermi level is key to the observation of Knight shifts).[49,52,53] The distributions of Knight shifts arise from Zn sites that vary in both their structure and their *s*-character. Those nearest to the core of the NC likely exhibit the largest Knight shifts due to the absence of both oxygen vacancies (V_O sites) and ligands. Conversely, those Zn sites at the surface either have a minimal or no Knight shift, due to pinning of free carriers in the NC due to surface traps, spinel microinclusions, f-center formations, and other defects—these are indicated by the rightmost, low-frequency edge of the powder pattern, which is similar to that of the undoped ZnO NCs.[17,18,49] Hence, in theory, the ratio of the Knight-shifted signal to unshifted signal can be used as a rough indicator of the degree of carrier deactivation for each sample.

Hence, to summarize the analysis above, the increasing concentrations of Al^{3+} dopants in the 0.9, 2.1, and 4.3 mol % AZO NC samples correspond to increased Knight shifts in the ^{67}Zn SSNMR spectra (with the largest being that of the 4.3 mol % sample), which can be attributed to increased generation of free carriers as the percentage of Al^{3+} incorporation increases. At 9.6 mol %, the Knight shifted feature is diminished with respect to that of the 4.3 mol % sample, indicating a reduced carrier density. This nonlinear relationship between carrier density and concentration is mirrored in the LSPR data (Table 1).

In the ^{67}Zn SSNMR spectra of the GZO series (Figure 2B), a similar Knight shift broadening is also observed. The Knight shift increases with dopant concentration, with maximum pattern intensity and breadth of *ca.* 350 ppm (*ca.* 18 kHz at 19.6 T) for the 10.3 mol % sample, and the highest Knight shifted frequency is similar to that of AZO (K_{iso}^{max} = 25186 Hz (485 ppm) and ΔK = 0.048%). However, the Knight shifts do not diminish at higher dopant concentrations to the degree observed for the AZO series.

The presence of Knight shifted signals that change in intensity with dopant concentration is indicative of a Fermi-gas-like behavior in the conduction band in both the AZO and GZO series of samples. The correspondence of free carrier densities to the presence of Knight shifts can be evaluated by consideration of the carrier densities determined from the SWIR LSPR extinction spectra and fits using the Extended Drude Model (Table 1, Figure S7).

In the AZO NC series, the highest carrier density (n) and corresponding plasma and LSPR shifts (ω_p and ω_{LSPR}) are observed for the 4.3 mol % sample, with a small decrease in carrier density for the 9.3 mol % AZO sample (Table 1). This is consistent with the largest Knight shift distribution for the 4.3 mol % AZO sample and a decrease in Knight shift breadth and intensity at higher dopant concentrations. These concomitant results may reflect generation of Al(III)-V_O-Al(III) pairs in the interstitial octahedral hollows in the ZnO lattice and oxygen vacancies in the lattice T_d sites (V_O), reminiscent of a spinel inclusion leading to Al^{3+} donors that reduce the carrier density, a phenomenon reported by Strouse and co-workers.[54]

In the GZO NC series, the values of n and ω_{LSPR} are also observed to increase with increasing Ga^{3+} concentrations (Table 1), again consistent with increases in the Knight shifted signal observed in the ^{67}Zn SSNMR spectra. It is worth noting

https://doi.org/10.1021/acs.chemmater.5c00496
Chem. Mater. 2025, 37, 6962−6973

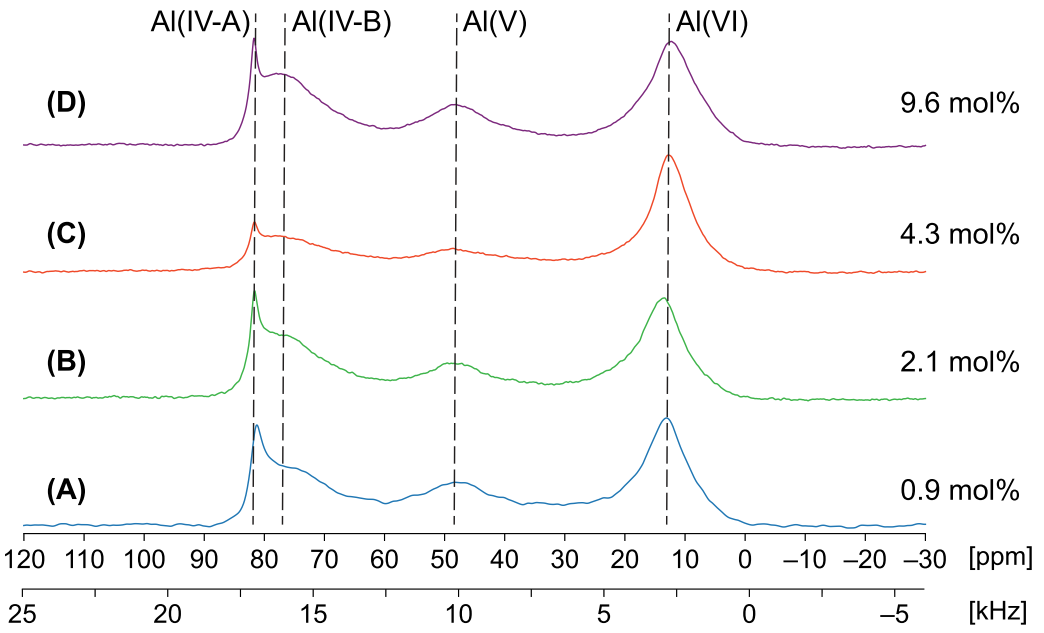

Figure 3. ^{27}Al Hahn-echo spectra of AZO NCs at varying doping levels acquired at 18.8 T under MAS conditions (ν_{rot} = 12 kHz).

Scheme 1. Four Types of Dopant Incorporation Commonly Observed in Metal-Doped Zinc Oxide NCs[a]

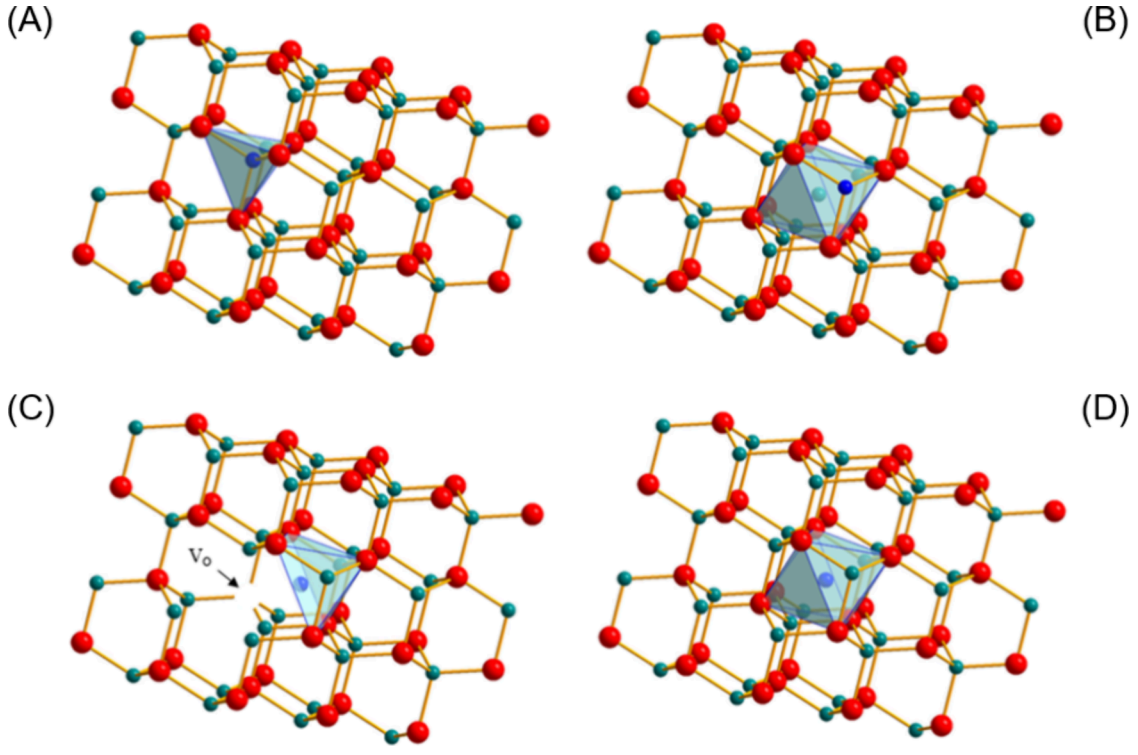

[a]Red spheres = O, turquoise spheres = Zn, blue spheres = Al. (A) Substitutional Al^{3+} (i.e., Al^{3+} substituting for Zn^{2+}, Al_{Zn}), (B) substitutional Al^{3+}–interstitial Zn^{2+} (Al_{Zn}-Zn_i), (C) Al^{3+}–interstitial O vacancy (Al_i-V_O), (D) interstitial Al^{3+} (Al_i). Reproduced from reference 56. Copyright 2019 American Chemical Society.

that at the highest Ga^{3+} incorporation, the calculated carrier densities begin to deviate from the linear trend, suggesting the possible onset of Ga(III)-V_O-Ga(III) spinel-like inclusions, leading to partial carrier deactivation in analogy to the above observations for AZO (though to a lesser degree). The Knight shift and LSPR data are consistent with a higher concentration of Ga^{3+} at the Zn-T_d lattice site relative Al^{3+}, perhaps reflecting a better size match between the Ga^{3+} and Zn^{2+} centers ($r_{ionic}(Ga^{3+})$ = 0.61 Å and $r_{ionic}(Al^{3+})$ = 0.53 Å, $r_{ionic}(Zn^{2+})$ = 0.74 Å).[55]

3.2.4. Distributions of Knight Shifts in the ^{67}Zn SSNMR Spectra. The range of Knight shifts, ΔK, is often insufficient for describing the nature of powder patterns influenced by a distribution of K_{iso}, since there are often variations in signal intensity across their breadths. To better describe such patterns, parameters describing deviations from a normal

https://doi.org/10.1021/acs.chemmater.5c00496
Chem. Mater. 2025, 37, 6962−6973

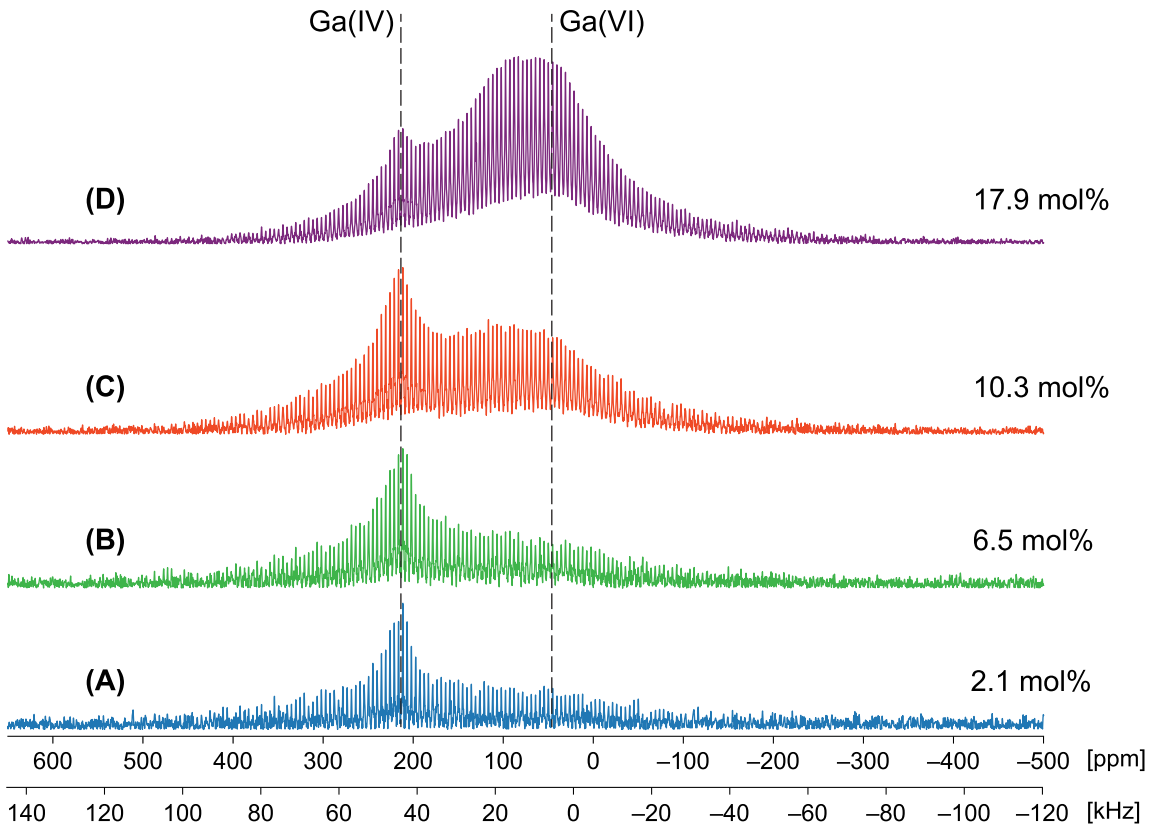

Figure 4. ^{71}Ga QCPMG NMR spectra of GZO NCs at varying doping levels acquired at 18.8 T under static conditions.

distribution can be used, which include the skewness (γ) and kurtosis (γ_2), which describe pattern asymmetry and intensity variation across the pattern, respectively (see Supplement S2; *N.B.*: the excess kurtosis, $\gamma_2 - 3$, is sometimes used in place of γ_2, since a normal distribution is indicated by $\gamma_2 - 3 = 0$). The combination of these values allows for a more detailed analysis of the relationship between observed Knight shifts and the inhomogeneous distribution of free carriers. It is noted that herein, skewness and kurtosis values are opposite in sign from how they are typically reported, as the chemical shift axis is plotted from positive to negative from left to right. Herein, positive and negative values of γ indicate distributions skewed to the left and right of the median, respectively.

The AZO NC series is considered first (Table 2, Figures S8–S11). For the 0.9, 2.1, and 9.6 mol % samples, the K_{iso}^{max}, γ, and γ_2 are all similar to one another. The $\gamma \approx 0.40$ indicates a small skew of the Knight shift distribution to high frequency, with the $\gamma_2 \geq 3.97$ indicative of low intensity in the high frequency region. This indicates a highly leptokurtic distribution (i.e., a statistical distribution with a sharp central peak and heavy tails). The 4.3 mol % sample is unique, due to not only its higher K_{iso}^{max} and larger ΔK, but also its larger γ = 1.01 and its distinct γ_2 = 3.79, which indicate an increased skewness to high frequency along with increased intensity in the high frequency region relative to that of the low frequency region.

The GZO series of samples exhibits different behavior (Figures S12–S15). For all of the samples, the K_{iso}^{max} and ΔK are similar but are significantly larger than those of the AZO series of samples. The γ and γ_2 values of the 2.1 and 6.5 mol % samples are similar to those of the 4.3 mol % AZO sample. The corresponding values for the 10.3 and 17.9 mol % samples are also indicative of highly skewed patterns, though with more evenly distributed intensities (i.e., as indicated by the values of γ_2 approaching 3.0). The significant increases in intensities in the high-frequency tails of these patterns are indicative of higher relative populations of Zn sites influenced by Knight shifts, which in turn corresponds to an increase in carrier densities within the NC core.

3.2.5. ^{27}Al SSNMR: Dopant Incorporation in AZO Samples. ^{27}Al SSNMR was used to gain insight into the lattice site occupation for Al^{3+} in ZnO NCs (i.e., four-, five-, and/or six-coordinate) as a function of dopant concentration. In all of the ^{27}Al MAS NMR spectra (Figure 3), there are four distinct features with unique chemical shifts: (i) a narrow peak centered at 82 ppm, (ii) a broad asymmetric pattern with its highest intensity near 78 ppm, (iii) a very broad pattern centered at 48 ppm, and (iv) a symmetric pattern of intermediate breadth centered at 14 ppm. The assignment of the sites can be made based upon the well-known chemical shift behavior for aluminum oxide materials,[44] the work of Sun et al. that reported multiple coordination environments for the Al^{3+} ion in their studies of doped ZnO ceramics,[56] and the established relationships between Platonic symmetry and the magnitude of quadrupolar interactions.[57] With reference to Scheme 1, the peaks and powder patterns can be assigned to Al^{3+} sites that are either substitutional (i.e., replacement of a four-coordinate Zn^{2+} site) or interstitial (i.e., occupation of a nominally six-coordinate site), as indicated by subscripts Zn and i, respectively.[58] The assignments based on the centers of gravity of the patterns (summarized in Table S6) are (i) Al(IV-A) substitutional (Al_{Zn}, 82 ppm), (ii) Al(IV-B) substitutional (Al^{3+} in the presence of an interstitial Zn^{2+} atom occupying a six-coordinate site, Al_{Zn}-Zn_i, 78 ppm), (iii) Al(V) interstitial

https://doi.org/10.1021/acs.chemmater.5c00496
Chem. Mater. 2025, 37, 6962−6973

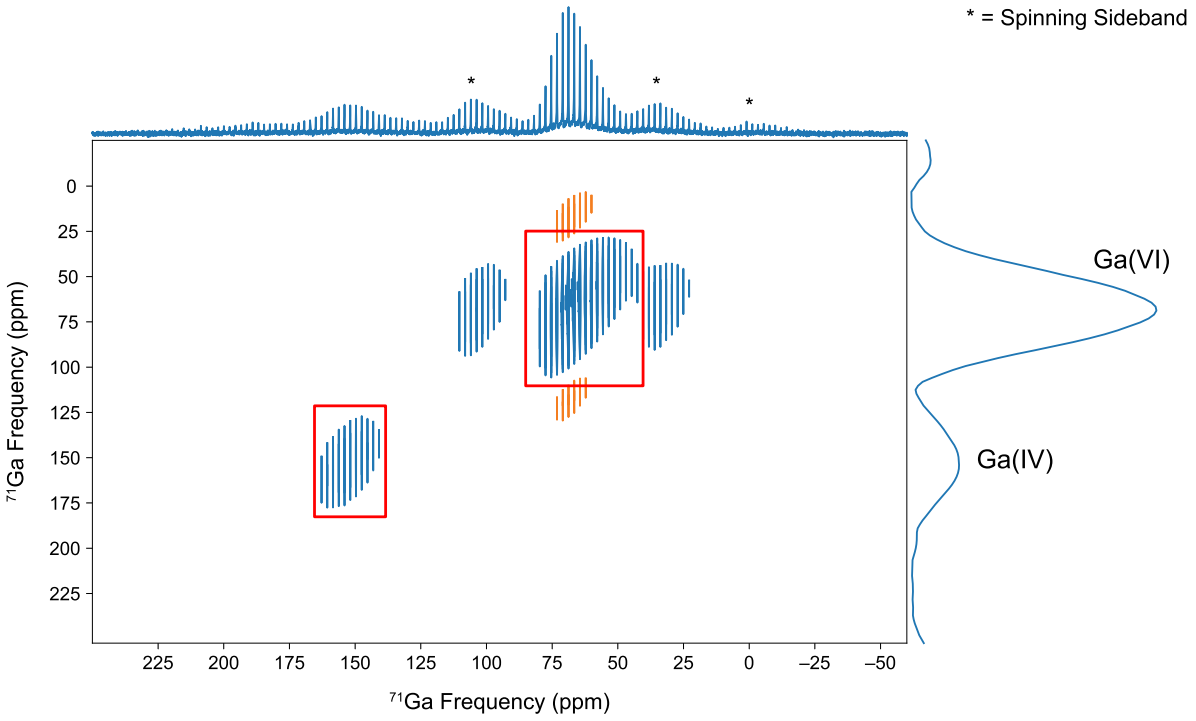

Figure 5. ^{71}Ga QMAT spectrum of 17.9 mol % GZO acquired at 35.2 T under MAS conditions (ν_{rot} = 16 kHz). Contours outlined in red boxes correspond to the Ga(IV) and Ga(VI) isotropic centerbands. The blue contours on either side of the Ga(VI) isotropic shifts are spinning sidebands, and the orange contours are believed to arise from residual signal that is out of phase with those of the isotropic resonances.

(Al^{3+} in the nominally six-coordinate site but with one oxygen vacancy, Al_i-V_O, 48 ppm), and (iv) Al(VI) interstitial (Al^{3+} in the six-coordinate site, Al_i, 14 ppm).[56] The presence of the feature centered at 48 ppm was initially unexpected, as a defect-free wurtzite structure does not have any conventional five-coordinate sites, nor does the normal or inverse spinel; hence, site features Al^{3+} coordination to five O atoms, though in a six-coordinate spinel-like site at an oxygen vacancy, a defect that is known to regularly occur in ZnO.[59,60]

Only Al(IV-A) has only a sharp resonance, indicating an environment of tetrahedral symmetry. The remainder of the sites all have considerably broader patterns, in part due to the spherically asymmetric (non-Platonic) Al^{3+} environments that result in larger values of C_Q (i.e., the Al(V) site is expected to have the largest value of C_Q). Furthermore, sharp features are missing from these patterns, reflecting positional disorder at these positions, which results in distributions of C_Q, η_Q, and δ_{iso} values. In the spectra of the 0.9, 2.1, and 9.6 mol % samples (Figures 3A, 3B, and 3D, respectively), the relative integrated intensities of the patterns are approximately equal (0.2:2.5:2.5:3.0). In the 4.3 mol % sample (Figure 3C) the ratio of integrated intensities is (0.1:1.4:2.1:3.0) (deconvolutions shown in Figure S16), meaning that the relative integrated intensity of the pattern corresponding to Al(VI) is increased with respect to that of Al(V), whereas those of Al(IVA) and Al(IVB) are diminished with respect to this same pattern. This indicates increased and decreased relative populations of six- and four-coordinate sites, respectively, with respect to those of all of the other samples. The notable change in the contribution of the features that arise between 2.1 to 4.3% may reflect the onset of lattice disorder arising from solubility limits for Al^{3+} in the ZnO lattice that leads Al(III)-V_O-Al(III) spinel-like inclusions,[14] which would explain the observed increase in six-coordinate Al^{3+} sites. It is noted that the relative intensities are coarsely estimated using four second-order quadrupolar patterns with varying degrees of Gaussian broadening; this is because absolute intensities of the peaks are difficult to quantify since iterative Czjzek fitting routines were unsuccessful in each case, perhaps due to issues of insufficiently high signal-to-noise and/or underlying signal that confounded the Czjzek algorithm. Given that the 4.3 mol % sample also has the largest Knight shifts in its ^{67}Zn spectrum (Figure 2A), and therefore the largest carrier densities, it is possible that the Al^{3+} dopants at these sites play a role in determining the nature of the LSPR, but only at this specific concentration. Finally, it is worth noting that Knight shifts are not observed in the spectra of dopants (i.e., the ^{27}Al and ^{71}Ga (*vide infra*) spectra of AZO and GZO, respectively) because the ZnO conduction band has very little contribution from dopant *s*-orbitals.[61]

3.2.6. ^{71}Ga SSNMR: Dopant Incorporation in GZO Samples. ^{71}Ga SSNMR was used to investigate the GZO series of NCs for similar purposes. ^{71}Ga chemical shifts follow a similar ordering to those of ^{27}Al (i.e., δ_{iso}(IV) > δ_{iso}(V) > δ_{iso}(VI)) (summarized in Table S7).[62] However, even though the nuclear quadrupole moment (Q) of ^{71}Ga is smaller than that of ^{27}Al ($Q(^{71}Ga)$ = 10.7 fm^2 vs $Q(^{27}Al)$ = 14.66 fm^2),[63] the lower nuclear spin of ^{71}Ga (I = 3/2) results in CT patterns that are substantially broader than those of ^{27}Al (I = 5/2).[32]

The ^{71}Ga QCPMG NMR spectra of the GZO samples are compared in Figure 4 (*N.B.*: they are processed in spikelet mode to enhance the S/N, as in the case of the ^{67}Zn QCPMG NMR spectra above). The spectrum of the 2.1 mol % sample (Figure 4A) has a narrow feature centered near 210 ppm, as well as a broad pattern that is skewed in the low-frequency direction. This stands in contrast to the ^{27}Al NMR spectra, where four distinct patterns are apparent at every dopant concentration. It is likely that most of this pattern corresponds

https://doi.org/10.1021/acs.chemmater.5c00496
Chem. Mater. 2025, 37, 6962−6973

to a CT pattern with a distribution of C_Q and η_Q values, with its chemical shift (as read approximately from the center of gravity, δ_{CG} = 210 ± 4 ppm) indicating a four-coordinate Ga^{3+} environment. Given the broadness and lack of sharp features, this pattern is similar to that of the Al(IV-B) site (Scheme 1); therefore, it is assigned as a Ga(IV-B) substitutional site (i.e., Ga^{3+} replaces Zn^{2+}, in the presence of an interstitial Zn^{2+} in a six-coordinate environment, Ga_{Zn}-Zn_i). It is possible that, in the 2.1 mol % sample, some of the signal corresponds to five- or six-coordinate sites; however, the S/N is too low to clearly identify the origin of these patterns.

As the Ga^{3+} concentration is increased, a second, very broad pattern emerges in the ^{71}Ga spectra (Figures 4B, 4C, and 4D) and increases in integrated intensity as the dopant concentration is increased. This pattern has a $\delta_{CG} \approx 75$ (±35) ppm that is evident for the 10.3 and 17.9 mol % samples (it may be present in Figures 4A and 4B, but it is not possible to discern this definitively due to the low S/N). This new pattern is tentatively assigned to a Ga(VI) site (i.e., Ga^{3+} in an interstitial environment, akin to Al(VI)). The large breadth of this pattern arises from a distribution of quadrupolar interactions, perhaps due to greater variation of positional disorder for Ga^{3+} ions in the six-coordinate sites in comparison to those in the four-coordinate sites. It is possible that some of the signal corresponds to a five-coordinate Ga(V) site akin to the Al(V) site; however, the S/N in the spectrum of the 17.9 mol % sample is not high enough to say this with certainty.

In order to interrogate the potential presence of the Ga(V) site, two sets of experiments were conducted using the 36 T Series Connected Hybrid (SCH) at MagLab (at 35.2 T, which corresponds to $\nu_0(^1H)$ = 1.5 GHz): (i) acquisition of 1D QCPMG spectra under both static and MAS conditions and (ii) the quadrupolar magic angle turning (QMAT) experiment.[35] In the former case, it was anticipated that the increased resolution resulting from the narrowing of the ^{71}Ga CT patterns would be enough to ascertain the presence of a Ga(V) site; however, this was not the case (Figure S17). In the latter case, the QMAT experiment greatly simplifies site assignment by separating the spinning sidebands in the SSNMR spectra of half-integer quadrupolar nuclei and yielding "infinite" MAS rate spectra in the indirect dimension that can be used to accurately determine EFG and CS tensor parameters (this experiment is especially useful when it is not possible to spin the sample faster than the breadth of the static powder pattern in kHz).[35] The ^{71}Ga QMAT NMR spectrum (Figure 5) reveals only two clear patterns in the indirect dimension, with centers of gravity at 210 and 75 ppm, which correspond to the Ga(IV) and Ga(VI) sites, respectively. Hence, there is no clear indication of the presence of a Ga(V) site in any of the ^{71}Ga SSNMR spectra.

These results indicate that the incorporation of Ga^{3+} in the GZO NCs with increasing doping levels is distinct from that of Al^{3+} in the AZO NCs. At low dopant levels, Ga^{3+} is incorporated in substitutional, four-coordinate Ga(IV) sites, whereas at higher dopant levels, Ga^{3+} preferentially occupies interstitial, six-coordinate Ga(VI) sites. As mentioned above, this distinct chemical behavior may arise from the difference in ionic radii of the Al^{3+} and Ga^{3+} ions.[55]

4. CONCLUSIONS

In this work, multinuclear SSNMR spectroscopy of quadrupolar nuclei, in tandem with other analytical methods, is used to characterize the structures of ZnO NCs doped with Group IIIA elements (i.e., Al and Ga). ^{67}Zn SSNMR is used to compare the ZnO NC structure to that of the bulk, crystalline ZnO wurtzite phase, with spectra of the former exhibiting Knight shifts that vary with the doping levels of Al^{3+} and Ga^{3+}. The largest Knight shift distributions are observed in the ^{67}Zn SSNMR spectra of the 4.3 mol % AZO NCs and 10.3 mol % GZO NCs, whereas that of the 9.6 mol % AZO NCs are greatly reduced and that of the 17.9 mol % GZO NCs only decreases slightly. The SSNMR results correlate with the reduced carrier activation (Table 1) observed with increasing incorporation of Al^{3+} or Ga^{3+} into the ZnO crystal lattice. The KS and carrier activation results can be interpreted as strong evidence for the onset of Al(III)-V_O-Al(III) and Ga(III)-V_O-Ga(III) spinel-like inclusions that serve to reduce their carrier densities, though to a much greater degree in the AZO NCs.

The Knight shift distributions observed in the ^{67}Zn spectra for both AZO and GZO track well with the values of n and ω_{LSPR} determined from Drude model fitting of the mid-IR LSPR extinction spectra, suggesting that SSNMR spectra of metal nuclides provide a complementary qualitative probe of carrier densities. ^{27}Al and ^{71}Ga SSNMR spectra are used to study the coordination environments of the dopants and their relative populations, which are also dependent upon dopant concentrations. In both the AZO and GZO series of samples, it is observed that increased dopant concentrations lead to increased populations of Al^{3+} and Ga^{3+} in the six-coordinate sites, which also correspond to the samples with the largest Knight shift distributions and highest carrier densities (i.e., the 4.3 mol % AZO NCs and 10.3 and 17.9 mol % GZO NCs). This raises the intriguing possibility of being able to synthesize NPs with specific carrier densities based upon an understanding of the nature and concentrations of the dopant species.

Multinuclear SSNMR of quadrupolar nuclei in NPs can clearly provide insights into the SPF relationships, which is of great use to chemists, materials scientists, and engineers, who all continue to pursue the goal of rational design of NPs with tailored properties for optoelectronic and semiconducting devices, where detailed knowledge of the relationships between structure and the Fermi level are essential. We hope that this work encourages further studies of this kind on a wide range of semiconducting nanomaterials.

■ ASSOCIATED CONTENT

Supporting Information

The Supporting Information is available free of charge at https://pubs.acs.org/doi/10.1021/acs.chemmater.5c00496.

Experimental parameters for solid state NMR measurements, pXRD, XRF elemental analysis, UV−vis−NIR extinction spectra, Knight shift values, ^{27}Al NMR spectral deconvolution, and ^{71}Ga QCPMG data collected at 35.2T (PDF)

■ AUTHOR INFORMATION

Corresponding Authors

Geoffrey F. Strouse − *Department of Chemistry & Biochemistry, Florida State University, Tallahassee, Florida 32306, United States;* orcid.org/0000-0003-0841-282X; Email: strouse@chem.fsu.edu

Robert W. Schurko − *Department of Chemistry & Biochemistry, Florida State University, Tallahassee, Florida 32306, United States; National High Magnetic Field*

https://doi.org/10.1021/acs.chemmater.5c00496
Chem. Mater. 2025, 37, 6962−6973

Laboratory, Tallahassee, Florida 32310, United States; orcid.org/0000-0002-5093-400X; Email: rschurko@fsu.edu

Authors

Robert B. Smith − *Department of Chemistry & Biochemistry, Florida State University, Tallahassee, Florida 32306, United States; National High Magnetic Field Laboratory, Tallahassee, Florida 32310, United States;* orcid.org/0000-0003-0248-366X

Carl R. Conti, III − *Department of Chemistry & Biochemistry, Florida State University, Tallahassee, Florida 32306, United States;* orcid.org/0000-0001-6223-6025

Sarah D. Bennett − *Department of Chemistry & Biochemistry, Florida State University, Tallahassee, Florida 32306, United States;* orcid.org/0000-0001-8124-1049

Adam R. Altenhof − *Department of Chemistry & Biochemistry, Florida State University, Tallahassee, Florida 32306, United States; National High Magnetic Field Laboratory, Tallahassee, Florida 32310, United States;* Present Address: ETH Zurich, Sonneggstrasse 28, 8006 Zürich, Switzerland

Complete contact information is available at: https://pubs.acs.org/10.1021/acs.chemmater.5c00496

Author Contributions

[§]R.B.S. and C.R.C. contributed equally.

Notes

The authors declare no competing financial interest.

■ ACKNOWLEDGMENTS

R.W.S. and R.B.S. are grateful for research support from the National Science Foundation Chemical Measurement and Imaging Program, with partial cofunding from the Solid State and Materials Chemistry Program (NSF-2003854). We are grateful for support from The Florida State University and the National High Magnetic Field Laboratory (NHMFL), which is funded by the National Science Foundation Cooperative Agreement (DMR-1644779, DMR-2128556) and by the State of Florida. Probes and time on the 36 T SCH platform are made possible in part by the National Resource for Advanced NMR Technology (NIH RM1 GM148766). Some of the pulse sequences implemented herein were developed with support from the Department of Energy Basic Energy Sciences program (DE-SC0022310). G.F.S. wishes to thank the National Science Foundation (DMR-1905757) "Tuning Plasmonic and Magneto-Plasmonic Behavior in 4-d Transition Metal Doped Indium Oxide" for funding. We are also grateful to Drs. Ivan Hung and Zhehong Gan for assistance with experiments on the 36 T SCH, Mr. Jason Kitchen for making tuning cards configured for ^{27}Al and ^{71}Ga, Dr. Xinsong Lin for assistance with acquisition of pXRD patterns, and Catherine Fabiano for assistance with FTIR data.

■ REFERENCES

(1) Casabianca, L. B. Solid-state nuclear magnetic resonance studies of nanoparticles. *Solid State Nucl. Magn. Reson.* **2020**, *107*, 101664−101671.

(2) Biswas, P.; Wu, C. Y. Nanoparticles and the Environment. *J. Air Waste Manag. Assoc.* **2005**, *55*, 708−746.

(3) Poole, C. P.; Owens, F. J. *Introduction to Nanotechnology*; Wiley: Hoboken, NJ, 2003.

(4) Astruc, D. Nanoparticles in Catalysis. *Chem. Rev.* **2020**, *120*, 461−463.

(5) Rampino, L. D.; Nord, F. F. Preparation of Palladium and Platinum Synthetic High Polymer Catalysts and the Relationship between Particle Size and Rate of Hydrogenation. *J. Am. Chem. Soc.* **1941**, *63*, 2745−2749.

(6) Huang, C.-H.; Tsourkas, A. Gd-based Macromolecules and Nanoparticles as Magnetic Resonance Contrast Agents for Molecular Imaging. *Curr. Top. Med. Chem.* **2013**, *13*, 411−421.

(7) Hui, Y.; Yi, X.; Hou, F.; Wibowo, D.; Zhang, F.; Zhao, D.; Gao, H.; Zhao, C. X. Role of Nanoparticle Mechanical Properties in Cancer Drug Delivery. *ACS Nano* **2019**, *13*, 7410−7424.

(8) Janotti, A.; Van de Walle, C. G. Fundamentals of zinc oxide as a semiconductor. *Rep. Prog. Phys.* **2009**, *72*, No. 126501.

(9) Broadway, D. A.; Dontschuk, N.; Tsai, A.; Lillie, S. E.; Lew, C. T. K.; McCallum, J. C.; Johnson, B. C.; Doherty, M. W.; Stacey, A.; Hollenberg, L. C. L.; Tetienne, J. P. Spatial mapping of band bending in semiconductor devices using in situ quantum sensors. *Nat. Electron.* **2018**, *1*, 502−507.

(10) Buonsanti, R.; Llordes, A.; Aloni, S.; Helms, B. A.; Milliron, D. J. Tunable Infrared Absorption and Visible Transparency of Colloidal Aluminum-Doped Zinc Oxide Nanocrystals. *Nano Lett.* **2011**, *11*, 4706−4710.

(11) Della Gaspera, E.; Chesman, A. S. R.; Van Embden, J.; Jasieniak, J. J. Non-injection Synthesis of Doped Zinc Oxide Plasmonic Nanocrystals. *ACS Nano* **2014**, *8*, 9154−9163.

(12) Muth, J. F.; Kolbas, R. M.; Sharma, A. K.; Oktyabrsky, S.; Narayan, J. Excitonic structure and absorption coefficient measurements of ZnO single crystal epitaxial films deposited by pulsed laser deposition. *J. Appl. Phys.* **1999**, *85*, 7884−7887.

(13) Johns, R. W.; Bechtel, H. A.; Runnerstrom, E. L.; Agrawal, A.; Lounis, S. D.; Milliron, D. J. Direct observation of narrow mid-infrared plasmon linewidths of single metal oxide nanocrystals. *Nat. Commun.* **2016**, *7*, 1−6.

(14) Conti, C. R.; McBride, J. R.; Strouse, G. F. Examining the Effect of Dopant Ionic Radius on Plasmonic M:ZnO Nanocrystals (M = Al^{3+}, Ga^{3+}, In^{3+}). *J. Phys. Chem. C* **2021**, *125*, 7772−7779.

(15) Davidowski, S. K.; Holland, G. P. Solid-State NMR Characterization of Mixed Phosphonic Acid Ligand Binding and Organization on Silica Nanoparticles. *Langmuir.* **2016**, *32*, 3253−3261.

(16) Knight, W. D. Nuclear Magnetic Resonance Shift in Metals. *Phys. Rev.* **1949**, *76*, 1259−1260.

(17) Slichter, C. P. The Knight shift − a powerful probe of condensed-matter systems. *Philos. Mag. B* **1999**, *79*, 1253−1261.

(18) Rhodes, H. E.; Wang, P. K.; Stokes, H. T.; Slichter, C. P.; Sinfelt, J. H. NMR of platinum catalysts I. Line shapes. *Phys. Rev. B* **1982**, *26*, 3559−3568.

(19) Bennett, L. H.; Watson, R. E.; Carter, G. C. Relevance of Knight Shift Measurements to the Electronic Density of States. *J. Res. Natl. Bur. Stand. A Phys. Chem.* **1970**, *74A*, 569−610.

(20) Marbella, L. E.; Millstone, J. E. NMR Techniques for Noble Metal Nanoparticles. *Chem. Mater.* **2015**, *27*, 2721−2739.

(21) Conti, C. R.; Quiroz-Delfi, G.; Schwarck, J. S.; Chen, B.; Strouse, G. F. Carrier Density, Effective Mass, and Nuclear Relaxation Pathways in Plasmonic Sn:In_2O_3 Nanocrystals. *J. Phys. Chem. C* **2020**, *124*, 28220−28229.

(22) Marbella, L. E.; Gan, X. Y.; Kaseman, D. C.; Millstone, J. E. Correlating Carrier Density and Emergent Plasmonic Features in $Cu_{2-x}Se$ Nanoparticles. *Nano Lett.* **2017**, *17*, 2414−2419.

(23) Levin, E. M. Effects of Ge substitution in GeTe by Ag or Sb on the Seebeck coefficient and carrier concentration derived from ^{125}Te NMR. *Phys. Rev. B* **2016**, *93*, 1−6.

(24) Levin, E. M.; Cook, B. A.; Ahn, K.; Kanatzidis, M. G.; Schmidt-Rohr, K. Electronic inhomogeneity and Ag:Sb imbalance of $Ag_{1-y}Pb_{18}Sb_{1+z}Te_{20}$ high-performance thermoelectrics elucidated by ^{125}Te and ^{207}Pb NMR. *Phys. Rev. B* **2009**, *80*, 115211−115217.

(25) Ortega, R. E.; Smith, R. B.; Kuszynski, J. E.; Bayles, A.; McGill, S. A.; Halas, N. J.; Schurko, R. W.; Strouse, G. F. Observing Metallic

Carriers in Highly Faceted Plasmonic Cd_2SnO_4 Inverse Spinel Nanocrystals. *Adv. Opt. Mater.* **2024**, *12*, 1−12.
(26) Rachkov, A. G.; Chalek, K.; Yin, H.; Xu, M.; Holland, G. P.; Schimpf, A. M. Redox Chemistries for Vacancy Modulation in Plasmonic Copper Phosphide Nanocrystals. *ACS Nano* **2024**, *18*, 5282−5296.
(27) Wainer, P.; Kendall, O.; Lamb, A.; Barrow, S. J.; Tricoli, A.; Gómez, D. E.; Van Embden, J.; Della Gaspera, E. Continuous Growth Synthesis of Zinc Oxide Nanocrystals with Tunable Size and Doping. *Chem. Mater.* **2019**, *31*, 9604−9613.
(28) Mendelsberg, R. J.; Garcia, G.; Milliron, D. J. Extracting reliable electronic properties from transmission spectra of indium tin oxide thin films and nanocrystal films by careful application of the Drude theory. *J. Appl. Phys.* **2012**, *111*, 063515−063524.
(29) Gan, Z.; Hung, I.; Wang, X.; Paulino, J.; Wu, G.; Litvak, I. M.; Gor'kov, P. L.; Brey, W. W.; Lendi, P.; Schiano, J. L.; Bird, M. D.; Dixon, I. R.; Toth, J.; Boebinger, G. S.; Cross, T. A. NMR spectroscopy up to 35.2 T using a series-connected hybrid magnet. *J. Magn. Reson.* **2017**, *284*, 125−136.
(30) Carr, H. Y.; Purcell, E. M. Effects of Diffusion on Free Precession in Nuclear Magnetic Resonance Experiments. *Phys. Rev.* **1954**, *94*, 630−638.
(31) Meiboom, S.; Gill, D. Modified Spin-Echo Method for Measuring Nuclear Relaxation Times. *Rev. Sci. Instrum.* **1958**, *29*, 688−691.
(32) Kentgens, A. P. M. A practical guide to solid-state NMR of half-integer quadrupolar nuclei with some applications to disordered systems. *Geoderma.* **1997**, *80*, 271−306.
(33) Hung, I.; Gan, Z. On the practical aspects of recording wideline QCPMG NMR spectra. *J. Magn. Reson.* **2010**, *204*, 256−265.
(34) Hahn, E. L. Spin Echoes. *Phys. Rev.* **1950**, *80*, 580−594.
(35) Hung, I.; Gan, Z. A magic-angle turning NMR experiment for separating spinning sidebands of half-integer quadrupolar nuclei. *Chem. Phys. Lett.* **2010**, *496*, 162−166.
(36) van Meerten, S. G. J.; Franssen, W. M. J.; Kentgens, A. P. M. ssNake: A cross-platform open-source NMR data processing and fitting application. *J. Magn. Reson.* **2019**, *301*, 56−66.
(37) Cho, S. H.; Ghosh, S.; Berkson, Z. J.; Hachtel, J. A.; Shi, J.; Zhao, X.; Reimnitz, L. C.; Dahlman, C. J.; Ho, Y.; Yang, A.; Liu, Y.; Idrobo, J.; Chmelka, B. F.; Milliron, D. J. Syntheses of Colloidal $F:In_2O_3$ Cubes: Fluorine-Induced Faceting and Infrared Plasmonic Response. *Chem. Mater.* **2019**, *31*, 2661−2676.
(38) Huang, Y.; Sutrisno, A. Recent Advances in Solid-State ^{67}Zn NMR Studies: From Nanoparticles to Biological Systems. *Annu. Rep. NMR Spectrosc.* **2014**, *81*, 1−46.
(39) Ohashi, R.; Sato, W.; Mizuno, M.; Ohki, S.; Deguchi, K.; Tansho, M.; Shimizu, T. Investigation of the effects of sintering and indium-doping of zinc oxide using ^{67}Zn magic angle spinning NMR analysis. *Solid State Nucl. Magn. Reson.* **2018**, *95*, 12−16.
(40) Caër, G. Le; Bureau, B.; Massiot, D. An extension of the Czjzek model for the distributions of electric field gradients in disordered solids and an application to NMR spectra of ^{71}Ga in chalcogenide glasses. *J. Phys.: Condens. Matter* **2010**, *22*, 065402−065419.
(41) Lovingood, D. D.; Achey, R.; Paravastu, A. K.; Strouse, G. F. Size- and Site-Dependent Reconstruction in CdSe QDs Evidenced by ^{77}Se{^{1}H} CP-MAS NMR Spectroscopy. *J. Am. Chem. Soc.* **2010**, *132*, 3344−3354.
(42) Cadars, S.; Smith, B. J.; Epping, J. D.; Acharya, S.; Belman, N.; Golan, Y.; Chmelka, B. F. Atomic Positional Versus Electronic Order in Semiconducting ZnSe Nanoparticles. *Phys. Rev. Lett.* **2009**, *103*, 3−6.
(43) Tandon, B.; Agrawal, A.; Heo, S.; Milliron, D. J. Competition between Depletion Effects and Coupling in the Plasmon Modulation of Doped Metal Oxide Nanocrystals. *Nano Lett.* **2019**, *19*, 2012−2019.
(44) Smith, M. E.; MacKenzie, K. J. D. *Multinuclear SSNMR of Inorganic Materials*, 1st ed.; Pergamon: Oxford, United Kingdom, 2002.
(45) d'Espinose de Lacaillerie, J. B.; Fretigny, C.; Massiot, D. MAS NMR spectra of quadrupolar nuclei in disordered solids: The Czjzek model. *J. Magn. Reson.* **2008**, *192*, 244−251.
(46) Wu, G. Zinc-67 nuclear magnetic resonance spectroscopy of solids. *Chem. Phys. Lett.* **1998**, *298*, 375−380.
(47) Werner-Zwanziger, U.; Paterson, A. L.; Zwanziger, J. W. The Czjzek distribution in solid-state NMR: Scaling properties of central and satellite transitions. *J. Non-Cryst. Solids* **2020**, *550*, 120383−120394.
(48) Spataro, G.; Champouret, Y.; Florian, P.; Coppel, Y.; Kahn, M. L. Multinuclear solid-state NMR study: a powerful tool for understanding the structure of ZnO hybrid nanoparticles. *Phys. Chem. Chem. Phys.* **2018**, *20*, 12413−12421.
(49) Nagashima, H.; Trébosc, J.; Kon, Y.; Sato, K.; Lafon, O.; Amoureux, J. P. Observation of Low-γ Quadrupolar Nuclei by Surface-Enhanced NMR Spectroscopy. *J. Am. Chem. Soc.* **2020**, *142*, 10659−10672.
(50) Knight, W. D.; Kobayashi, S.-I. Knight Shift. In *Encyclopedia of Magnetic Resonance*; John Wiley & Sons, Ltd.: Chichester, United Kingdom, 2007; pp 1−7.
(51) Bastow, T. J. ^{67}Zn NMR in zinc metal. *J. Phys.: Condens. Matter* **1996**, *8*, 11309−11315.
(52) Choi, Y. J.; Kang, K. M.; Park, H. H. Anion-controlled passivation effect of the atomic layer deposited ZnO films by F substitution to O-related defects on the electronic band structure for transparent contact layer of solar cell applications. *Sol. Energy Mater. Sol. Cells.* **2015**, *132*, 403−409.
(53) Ellmer, K.; Bikowski, A. Intrinsic and extrinsic doping of ZnO and ZnO alloys. *J. Phys. D: Appl. Phys.* **2016**, *49*, 413002−413035.
(54) Hardy, D. A.; Tigaa, R. A.; McBride, J. R.; Ortega, R. E.; Strouse, G. F. Structure-Function Correlation: Engineering High Quantum Yields in Down-Shifting Nanophosphors. *J. Am. Chem. Soc.* **2019**, *141*, 20416−20423.
(55) Xu, D.; Zhao, H.; Yu, T.; Duan, X.; Zhao, W. Effects of Li/M (M = Al, Ga, In, and Er) co-doping on the electrical properties of $BiFeO_3$−$BaTiO_3$ ceramics. *J. Mater. Sci.: Mater. Electron.* **2022**, *33*, 22736−22750.
(56) Sun, Q.; Tian, T.; Zheng, L.; Man, Z.; Li, G.; Barré, M.; Dittmer, J.; Bulou, A.; Kassiba, A. H. Electronic active defects and local order in doped ZnO ceramics inferred from EPR and ^{27}Al NMR investigations. *J. Eur. Ceram. Soc.* **2019**, *39*, 3070−3076.
(57) Autschbach, J.; Zheng, S.; Schurko, R. W. Analysis of Electric Field Gradient Tensors at Quadrupolar Nuclei in Common Structural Motifs. *Concepts Magn. Reson. A: Bridg. Educ. Res.* **2010**, *36*, 84−126.
(58) Wied, J. K.; Mockenhaupt, B.; Schurmann, U.; Kienle, L.; Mangelsen, S.; Glanzer, J.; Celinski, V. R.; Behrens, M.; Schmedt auf der Gunne, J. Method for Surface Characterization Using Solid-State Nuclear Magnetic Resonance Spectroscopy Demonstrated on Nanocrystalline ZnO:Al. *J. Anal. Chem.* **2024**, *96*, 11290−11298.
(59) Soriano, V.; Galland, D. Photosensitivity of the EPR Spectrum of the F^+ Center in ZnO. *Phys. Status Solidi B* **1976**, *77*, 739−743.
(60) Pellerin, N.; Dodane-Thiriet, C.; Montouillout, V.; Beauvy, M.; Massiot, D. Cation Sublattice Disorder Induced by Swift Heavy Ions in $MgAl_2O_4$ and $ZnAl_2O_4$ Spinels: ^{27}Al Solid-State NMR Study. *J. Phys. Chem. B* **2007**, *111*, 12707−12714.
(61) Mora-Fonz, D.; Buckeridge, J.; Logsdail, A. J.; Scanlon, D. O.; Sokol, A. A.; Woodley, S.; Catlow, C. R. A. Morphological Features and Band Bending at Nonpolar Surfaces of ZnO. *J. Phys. Chem. C* **2015**, *119*, 11598−11611.
(62) Walkley, B.; Provis, J. L. Solid-state nuclear magnetic resonance spectroscopy of cements. *Mater. Today Adv.* **2019**, *1*, 100007−100049.
(63) Pyykkö, P. Year-2017 nuclear quadrupole moments. *Mol. Phys.* **2018**, *116*, 1328−1338.

https://doi.org/10.1021/acs.chemmater.5c00496
Chem. Mater. 2025, 37, 6962−6973